Soil and atmospheric drought explain the biophysical conductance responses in diagnostic and prognostic evaporation models over two contrasting European forest sites

K. Mallick[1,2], M. Sulis[1], T. Hu[1], and C.D. Jiménez-Rodríguez[1]

[1]Remote Sensing and Natural Resources Modeling, Department ERIN, Luxembourg Institute of Science and Technology, Belvaux, Luxembourg.

[2]Biometeorology Lab, Department of Environmental Science, Policy and Management, University of California, Berkeley, California, United States.

Corresponding author: Kanishka Mallick (kaniska.mallick@gmail.com)

Key Points:

- Diagnostic (STIC1.2) and prognostic (CLM5.0) evaporation models show distinct levels of sensitivity to water stress.
- STIC1.2 and CLM5.0 evaporation models better agree in simulating the energy fluxes as compared to underlying biophysical conductance.
- Major differences in the simulated stomatal conductance are due to divergences in the physiological assumptions of the two evaporation modelling approaches.

Abstract

Diagnosing and predicting evaporation through satellite-based surface energy balance (SEB) and land surface models (LSMs) is challenging due to the non-linear responses of aerodynamic (g_a) and stomatal conductance (g_{cs}) to the coalition of soil and atmospheric drought. Despite a soaring popularity in refining g_{cs} formulation in the LSMs by introducing a link between soil-plant hydraulics and g_{cs}, the utility of g_{cs} has been surprisingly overlooked in SEB models due to the overriding emphasis on eliminating g_a uncertainties and the lack of coordination between these two different modeling communities. Therefore, a persistent challenge is to understand the reasons for divergent evaporation estimates from different models during strong soil-atmospheric drought. Here we present a virtual reality experiment over two contrasting European forest sites to understand the apparent sensitivity of the two critical conductances and evaporative fluxes to a water-stress factor (β-factor) in conjunction with land surface temperature (soil drought proxy) and vapor pressure deficit (atmospheric drought proxy) by using a non-parametric diagnostic model (Surface Temperature Initiated Closure, STIC1.2) and a prognostic model (Community Land Model, CLM5.0). Results revealed the β–factor and different functional forms of the two conductances to be a significant predictor of divergent response of the conductances to soil and atmospheric drought, which subsequently propagated in the evaporative flux estimates between STIC1.2 and CLM5.0. This analysis reaffirms the need for consensus on theory and models that capture the sensitivity of the biophysical conductances to the complex coalition of soil and atmospheric drought for better evaporation prediction.

Plain Language Summary

Water lost by plants through evaporation is strongly regulated by two important physical and biological attributes, namely aerodynamic and stomatal conductance. The magnitude and variability of these conductances and their degree of regulation on evaporation is heavily dependent on how the conductances respond to the conjugate dryness from the soil and the atmosphere. Because these conductances cannot be typically measured at a large scale, the majority of the global evaporation models use different mechanistic functions to estimate them, which involves many empirical parameters. Such methods do not fully capture the evaporation variability of ecosystems during water stress, leading to large errors in water cycle monitoring. Our model-based synthetic experiment shows how two structurally different models with different functional forms of the conductances respond very differently to emerging soil-atmospheric water stress and produce divergent estimates of evaporation in a variety of dry and wet conditions. While this study offers a greater insight into the role of conjugate effects of soil and atmospheric drought in explaining the conductances and evaporation variability, it also shows a novel perspective to reconcile predictive and remote sensing evaporation models for water management applications, testing theory of plant water use and land-atmosphere interactions.

1 Introduction

Soil and atmospheric droughts are triggered by enhanced land surface drying and climate warming. As a result, they feedback to some of the fundamental drivers of terrestrial evaporation namely, land surface temperature (LST) and atmospheric vapor pressure deficit (D_a), which subsequently affects climate and physiology of terrestrial ecosystems (Morrow and Friedl, 1998; Liao et al., 2020). While their coalition controls the magnitude and variability of the surface energy balance (SEB) components (Thakur et al., 2021, Mallick et al., 2022), they are simultaneously modulated by the SEB partitioning (Kustas and Anderson, 2009; Anderson et al., 2012; Mallick et al., 2018, 2022). LST is very sensitive to soil water content variations and captures additional information on the biophysical controls on surface temperature, such as evaporative cooling and stomatal conductance variations (Kustas and Anderson, 2009; Anderson et al., 2012; Mallick et al., 2016, 2022). While LST serves as a key diagnostic variable to monitoring land surface biophysical states (Green et al., 2022), it is also a prognostic indicator of their evolution under global warming and land use change (Chen and Dirmeyer, 2020). On the other hand, D_a is expected to rise over ecosystems due to the combination of increased LST, reduced soil water content, and decreased relative humidity due to low evaporation (Byrne & O'Gorman, 2013). An elevated D_a increases the atmospheric demand for evaporation (Monteith, 1965; Penman, 1948), and it simultaneously reduces (enhances) stomatal (aerodynamic) conductance (Damour et al., 2010; Medlyn et al., 2011; Mott, 2007). Therefore, understanding the conductance response to these two opposing effects of changes in D_a due to surface temperature warming is crucial for assessing the impacts of soil and atmospheric drought on evaporation for better water cycle assessment through different models (Massman et al., 2019).

LST-based diagnostic monitoring and mapping of evaporation varies from multiple spatio-temporal scales and involves a host of models (Bhattarai et al., 2018; 2019). The most common approach (Anderson et al., 2007) centres on assuming a physical model of evaporation in the framework of SEB and many of the variables required to compute evaporation using the SEB models are available directly as satellite products (e.g., vegetation index, albedo, leaf area index, vegetation cover). What is common to all the approaches is that they rely to a greater extent on parameterization of physical surface characteristics and plant biological attributes for deriving an estimate of evaporation. Two such important characteristics are the aerodynamic conductance and canopy-surface conductance and thus the diagnostic estimates of evaporation from the conventional approaches are conditional on their parameterizations (Kustas et al., 2016; Trebs et al., 2021). The current bottlenecks are that LST-based diagnostic approaches involve significant structural complexity with respect to parameterization of soil and aerodynamic conductance, the lack of a physically-based aerodynamic conductance model (Holwerda et al., 2012), and bypassing the role of LST versus stomatal conductance interactions in evaporation (Mallick et al., 2022).

LSMs are useful tools for predicting long-term records of LST across a wide range of spatial scales. These prognostic time series are iteratively computed by parameterizing the land surface energy fluxes using Monin-Obukhov similarity theory (e.g., Sellers et al., 1986). These time series have been exploited for investigating the role of LST in modulating the land surface energy partitioning (Gao et al., 2004; Zeng et al., 2012) and exploring the relationship between LST diurnal cycle and the degree of land-atmosphere coupling strength through multi-model experiments (Koster et al., 2004, 2006). The LSM-simulated LST records have been also

blended with thermal infrared (TIR) remote sensing data using various postprocessing techniques to obtain a complete spatiotemporal dataset that overcome the limitations of both prognostic and diagnostic LST information (Siemann et al., 2016; Long et al., 2020; Zhang et al., 2021). On the other hand, many previous validation and comparison studies based on the use of in-situ and remote sensing data have shown persistent limitations of LSMs in realistically simulating this essential climate variable of the Earth system (e.g., Mitchell et al., 2004; Zheng et al., 2012; Wang et al., 2014; Trigo et al., 2015, Koch et al., 2016). These systematic evaluations have led to continuous improvements in LSMs formulations related to the parameterized roughness length for heat (Chen et al., 2010), soil thermal conductivity (Zeng et al., 2012), and soil evaporation resistance (Ma et al., 2021). For instance, Yuan et al. (2021) used MODIS LST data product to validate a revised surface roughness scheme of the Common Land Model (CoLM). Similarly, Meier et al. (2022) verified a series of modifications of the surface roughness in the Community Land Model (version 5.1) by assessing the improvements in the simulated LST diurnal cycle for different land cover types. Despite the improved model performances and underpinning the prominent role of LST in the predictive skills of LSMs, it remains difficult to fully disentangle the processes and feedback mechanisms through which changes and biases in LST propagate into the simulated vegetation biophysical interactions.

Several studies have exploited the synergies between remote sensing-based evaporation models and Land Surface Models (LSMs) for acquiring a better understanding of land surface energy partitioning, land-atmosphere interactions, and couplings of the water-carbon cycles (Levine et al., 2016; Gevaert et al., 2017, among many others). These studies have employed LSMs of varying complexity and remote sensing-based products relying on diverse sources of information extracted from different spectral wavebands of satellite sensors. In this framework, Long et al. (2014) assessed the evaporation estimates from four different LSMs and two remote sensing products. They found that the uncertainty is lower in LSMs and that such uncertainty is resolution-dependent, with lower uncertainty at coarser spatial resolutions. Similar findings were reported by Wang et al. (2015) that compared the evaporation output from three different LSMs with an evaporation product based on MODIS data over Canada. Zhang et al. (2020) proposed a systematic evaluation and comparison of multiple evaporation data models over the contiguous United States. This effort was carried out within the North American Land Data Assimilation System (NLDAS) where multiple LSMs are integrated and compared against different remote sensing-based evapotranspiration products (e.g., GLEAM and MODIS-based dataset). Results of this study indicated a general agreement in the spatial patterns and seasonal evaporation of the different data output, despite a broad range of estimates within both prognostic and diagnostic class of models. Overall, these studies were critical to identifying strengths and weaknesses of the various evaporation products, providing guidelines for models' improvements and effective strategies to reduce uncertainties. However, none of these studies have compared the underlying biophysical interactions and feedback mechanisms explaining the link between evaporation, LST, and the associated conductances (i.e., aerodynamic, and stomatal) in diagnostic (i.e., remote sensing-based) and prognostic (i.e., LSMs) models. This is because most of the remote sensing-based evaporation models use surface parameterizations (i.e., surface roughness, atmospheric stability and conductances) that are very similar to those that are implemented in LSMs and that show limited predictive capabilities and high uncertainties (El Ghawi et al., 2023). This is an obvious limiting factor impeding an independent and stringent benchmarking of the inherent assumptions of prognostic and diagnostic evaporation models.

To summarize, while LST is used as a critical boundary condition to understand drought-induced variability in evaporation in the diagnostic models, D_a is used as an important boundary condition to understand both LST and evaporation variability in the prognostic models. The explanatory potential of evaporation variability in both the approaches depends on how well the biophysical conductances in the models respond to the coalition of soil and atmospheric drought. The present study introduces a virtual reality numerical framework where the non-parametric remote sensing evaporation model STIC1.2 (Mallick et al., 2018, 2022) is driven using two configurations: (i) LST signal simulated by the state-of-the-art LSM CLM5.0 (Lawrence et al. 2019); and (ii) LST retrieved from thermal infrared remote sensing data products. The latter are also used to assess the predictive skills of CLM5.0 in reproducing the LST under different plant water stress conditions. This numerical framework aims at comparing the role of LST magnitude and variability on the biophysical conductances in STIC1.2 and CLM5.0 and assessing the relative sensitivity of the biophysical conductances to LST and ancillary environmental variables in diagnostic (STIC1.2) and prognostic (CLM5.0) evaporation modeling approaches. The virtual reality framework is established at two forested sites in Europe, with contrasting environmental conditions, different plant functional types, and spanning a temporal length characterized by strong interannual climate variability.

2 Methods and Data

2.1 Study sites

This study considered two contrasting forested sites in Europe, namely Puéchabon (43.74°N, 3.60 °E, France, FR-Pue) and Loobos (52.17°N, 5.74°E, Netherlands, NL-Loo). FR-Pue site has a Mediterranean climate with a mean annual temperature of 13.8 °C and a mean annual precipitation of 914 mm yr^{-1}. The site is characterized by dry and hot summers reaching a maximum vapor pressure deficit of 6.0 kPa; Csa class according to the Köppen-Geiger classification (Beck et al., 2018). The site has a shallow soil layer (< 1m depth) with a clay loam texture (Reichstein et al., 2002) sitting on top of a hard limestone formation (Cabon et al., 2018). The vegetation cover is classified as evergreen broadleaf due to the dominance of *Quercus ilex* L. trees. NL-Loo site has a mean annual temperature of 10.0 °C and a mean annual precipitation of 754 mm yr^{-1}. This temperate climate is characterized by warm summers without a dry season and maximum vapor pressure deficit around 4.3 kPa; the site has an Oceanic climate (Cfb) following the Köppen-Geiger classification. The site is sitting on top of ice-pushed deposits giving origin to a sandy loam soil with more than 30 m of depth (Tiktak and Bouten, 1994). The land cover is evergreen needleleaf with *Pinus sylvestris* L. as the dominant tree species. The meteorological observations of these two sites were obtained from the FLUXNET2015 dataset (Pastorello et al., 2020), spanning over the 2001-2014 and 2002-2013 periods for FR-Pue and NL-Loo, respectively. These long-time records embed strong interannual variability including severe droughts as the 2003 continental and the 2006/2010 regional heat wave and drought events in Europe.

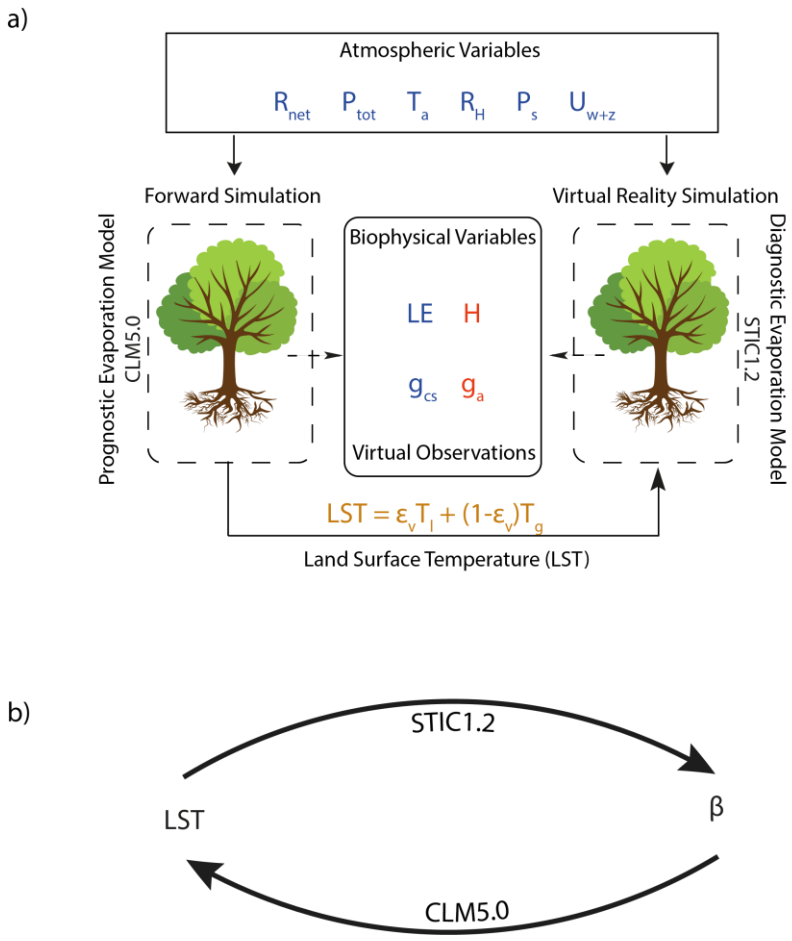

Figure 1. (a) Conceptual diagram of the virtual reality experiment. While the SEB fluxes and conductance outputs of forward simulation from CLM5.0 is used as virtual reality observation, LST output is further used to drive STIC1.2 simulation with the same environmental drivers. The fluxes and conductance outputs from STIC1.2 are subsequently analyzed with respect to the virtual reality. **(b)** Diagram illustrating the relationship between LST and simulated water stress factor in the diagnostic STIC1.2 and prognostic CLM5.0 approach.

2.2 Diagnostic and Prognostic Evaporation Models

2.2.1 Surface Temperature Initiated Closure – STIC1.2

STIC1.2 is a non-parametric evaporation model which perceives the vegetation-atmosphere system as a box and considers evaporation as both the driver and driven by different biophysical states in the vegetation-atmosphere system (Mallick et al., 2022). Assuming the surface-atmosphere exchange operates within the available environmental and water limits, STIC1.2 estimates evaporation by finding analytical solution of the biophysical conductances from the known boundary conditions of the box that is, solar radiation (R_g), air temperature (T_a), relative humidity (rH), and LST (Mallick et al., 2018, 2022; Trebs et al., 2021). The main biophysical states are the aerodynamic temperature, aerodynamic conductance, and canopy-surface conductance, respectively. Considering vegetation-soil-substrate as a single slab, STIC1.2 implicitly assumes the aerodynamic conductances from individual air-canopy and canopy-substrate components to be the 'effective' aerodynamic conductance for energy and

water vapor (i.e., g_a), and surface conductance from individual canopy (stomatal) and soil/substrate complexes to be the 'effective' canopy-surface conductance (i.e., g_{cs}) which simultaneously regulates the exchanges of sensible and latent heat fluxes between the surface and the atmosphere.

The explicit assumptions of STIC1.2 include the (a) first order dependence of evaporative fraction on water stress, g_a and g_{cs}; (b) direct feedback between water stress with g_a, and g_{cs} driven by LST sensitivity to water stress variations; and (c) STIC1.2 uses LST-air temperature difference in the model as a proxy of soil-vegetation water stress and assume that the difference between LST-air temperature can explain the soil moisture induced variability in conductances and fluxes.

By integrating LST with surface energy balance (SEB) theory and vegetation biophysical principles, STIC1.2 formulates multiple state equations to eliminate the need for any empirical parameterizations of the conductances. The state equations are related to LST through an aggregated water stress factor (I_{sm}) and the effects of LST are subsequently propagated into the analytical solutions of the conductances through the water stress (Supporting Information, in Mallick et al., 2022). The inputs needed for the computation of conductances and SEB fluxes in STIC1.2 are T_a, LST, rH or air vapor pressure (e_a), and downwelling and reflected global radiation (R_g and R_r).

2.2.2 Community Land Model version 5.0 – CLM5.0

CLM5.0 is a state-of-the-art LSM that simulates the land surface biogeophysical, biogeochemical, and hydrological processes that control the exchange of water, energy, and matter fluxes at the land-atmosphere interface. Here we provide a brief discussion of the key elements of CLM5.0 that are investigated in the virtual reality numerical framework, whilst a comprehensive description of the model structure can be found in Lawrence et al. (2019) and of the model formulations in the user manual documentation (Lawrence et al., 2018). The land surface energy fluxes, namely sensible and latent heat fluxes, are calculated using separated vegetation and ground surfaces and discriminating between shaded and sunlit vegetation components. The energy fluxes are calculated based on the Monin-Obukhov similarity theory through an iterative procedure solving for vegetation and ground temperature. In this procedure, the aerodynamic conductance, which expresses the efficiency of the turbulent transfer of heat, momentum, and water vapor is calculated as a function of plant-specific parameters (i.e., displacement height, roughness length) and adjusted according to atmospheric stability conditions. CLM5.0 uses the coupled stomatal conductance and photosynthesis model following Medlyn et al. (2011), where the leaf water potential calculated by the plant hydraulic system (Kennedy et al., 2019) serves as indicator for water stress conditions through an attenuation of the maximum carboxylation (biochemical limitation). The calculated leaf water potential is also used for the continuous update (in analogy to the soil characteristics curves) of plant hydraulic properties through the definition of a plant vulnerability curve for each segment (i.e., roots, xylem, and sunlit and shaded leaf segments) of the vegetated surface. For further details on the calculation of the water stress factor (β-factor) in the plant hydraulic system of CLM5.0 the reader is referred to Kennedy et al., (2019).

2.3 Virtual Reality Framework

The virtual reality framework is created by running the STIC1.2 model under two different configurations. In the first configuration (scenario-1), the LST simulated by CLM5.0 is used as virtual reality to drive the STIC1.2 model. The LST in CLM5.0 is computed based on the leaf temperature (T_{leaf}) and the temperature of the ground (T_{grnd}):

$$LST = \varepsilon_v T_{leaf} + (1 - \varepsilon_v) T_{grnd}$$

where the vegetation emissivity ε_v is calculated as function of the LAI, SAI, and the average inverse optical depth for longwave radiation (set to 1 in CLM5.0). All the variables are computed at hourly time steps.

In the second configuration (scenario-2), STIC1.2 is run in its default mode, with LST data from NASA MODIS onboard Aqua product (MYD21). The LST acquisition time of MODIS Aqua is 13.30 hrs local time and daily LST of MYD21 product (MYD21A1D) was used in the present analysis. In both configurations, STIC1.2 and CLM5.0 used the same atmospheric forcing preprocessed using the FLUXNETLSM v.1.0 R package (Ukkola et al., 2017). The results of the virtual reality are exploited to get a deeper understanding of the link between LST, D_a, and the land surface energy partitioning in the diagnostic (STIC1.2) and prognostic (CLM5.0) models. This link is explained through the analysis of the ratio between the stomata and aerodynamic conductance from both STIC1.2 and CLM5.0 and their controlling environmental drivers. The analysis of the results is consistently performed using the water stress factor of CLM5.0 (β) as a third variable to understand the agreement/disagreements between the conductances and fluxes from the two models for a wide range of atmospheric and plant water stress conditions. Furthermore, Partial Least Squares Regression (PLSR) is employed to identify fundamental relationships between the individual conductances and a host of model input variables. Regressions are made using the SIMPLS algorithm, which calculates PLS factors directly as linear combinations of the original variables (de Jong, 1993; Trebs et al., 2021) after normalization of all variables. To understand the degree of relationship between the input variables and the conductances, we derived the Variable Importance in Projection (VIP) scores based on the normalized PLS weights, scores, and loadings according to Trebs et al. (2021). A conceptual diagram of the virtual reality framework and the nature of the analysis is presented in Figure 1.

Three statistical metrics were used to assess the performances of LST, and latent and sensible heat flux:

$$r = \frac{\sum_{i=1}^{n}(E_i - \bar{E})\,(O_i - \bar{O})}{\sqrt{\sum_{i=1}^{n}(E_i - \bar{E})^2}\sqrt{\sum_{i=1}^{n}(O_i - \bar{O})^2}}$$

$$RMSD = \sqrt{\sum_{i=1}^{n}\frac{(E_i - O_i)^2}{n}}$$

$$bias = \sum_{i=1}^{n}\frac{E_i - O_i}{n}$$

where r is the Pearson's correlation coefficient, *RMSD* is root-mean-square difference, *bias* is the mean bias, between the model and measurements, n is the total number of data pairs. E_i and O_i are the model estimated and measured fluxes and is the average of measured values and is the average of estimated values. Additionally, the Kling-Gupta efficiency (KGE) is adopted to provide a quantitative and objective assessment of the agreement between the measured (virtual reality) and estimated surface energy balance fluxes (Gupta et al. 2009). It is calculated as follows:

$$KGE = 1 - \sqrt{(r-1)^2 + (\frac{\sigma_E}{\sigma_0} - 1)^2 + (\frac{\bar{E}}{\bar{O}} - 1)^2}$$

where r is the Pearson correlation coefficient, σ_0 and σ_E are the standard deviations of virtual reality and STIC1.2 estimates, respectively. The closer KGE is to 1, the more consistent are the STIC1.2 estimates with respect to the virtual reality.

3 Results and Discussion

3.1 Comparing CLM5.0 and MYD21A1D LST and SEB fluxes for a range of water stress

LST is one of the important boundary conditions that drives the biophysical conductances and fluxes in STIC1.2. Since CLM5.0 LST is used to drive STIC1.2 in scenario-1, a comparison of CLM5.0 LST with respect to a reference dataset is necessary. Therefore, we use the most recent version of MODIS (MODerate Resolution Imaging Spectroradiometer) on-board Aqua daily LST product (product name MYD21) as a reference data for such a comparison. LST estimates from CLM5.0 were significantly correlated (r = 0.95 – 0.96, p<0.05) with MYD21 retrievals (**Figure 2a - b**) for the simulated ranges of β, with a bias and systematic root mean square difference (sRMSD) of -0.35 – 2.35°C and 29 – 44%, respectively. While cold bias in CLM5.0 for LST>25°C corresponded to high soil and atmospheric water stress in the model (β: 0 – 0.25) in FR-Pue, a consistent warm bias in CLM5.0 LST was also evident for the entire range of β in NL-Loo.

(a) (b)

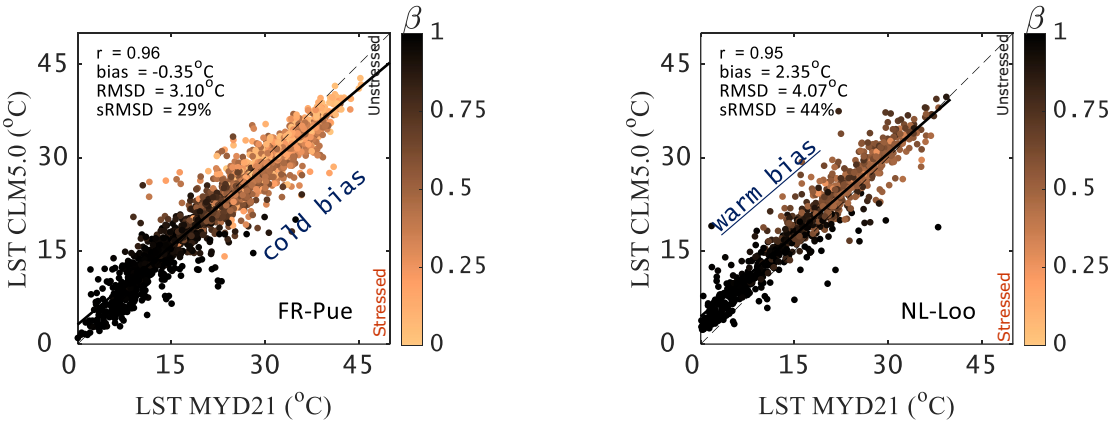

(c) (d)

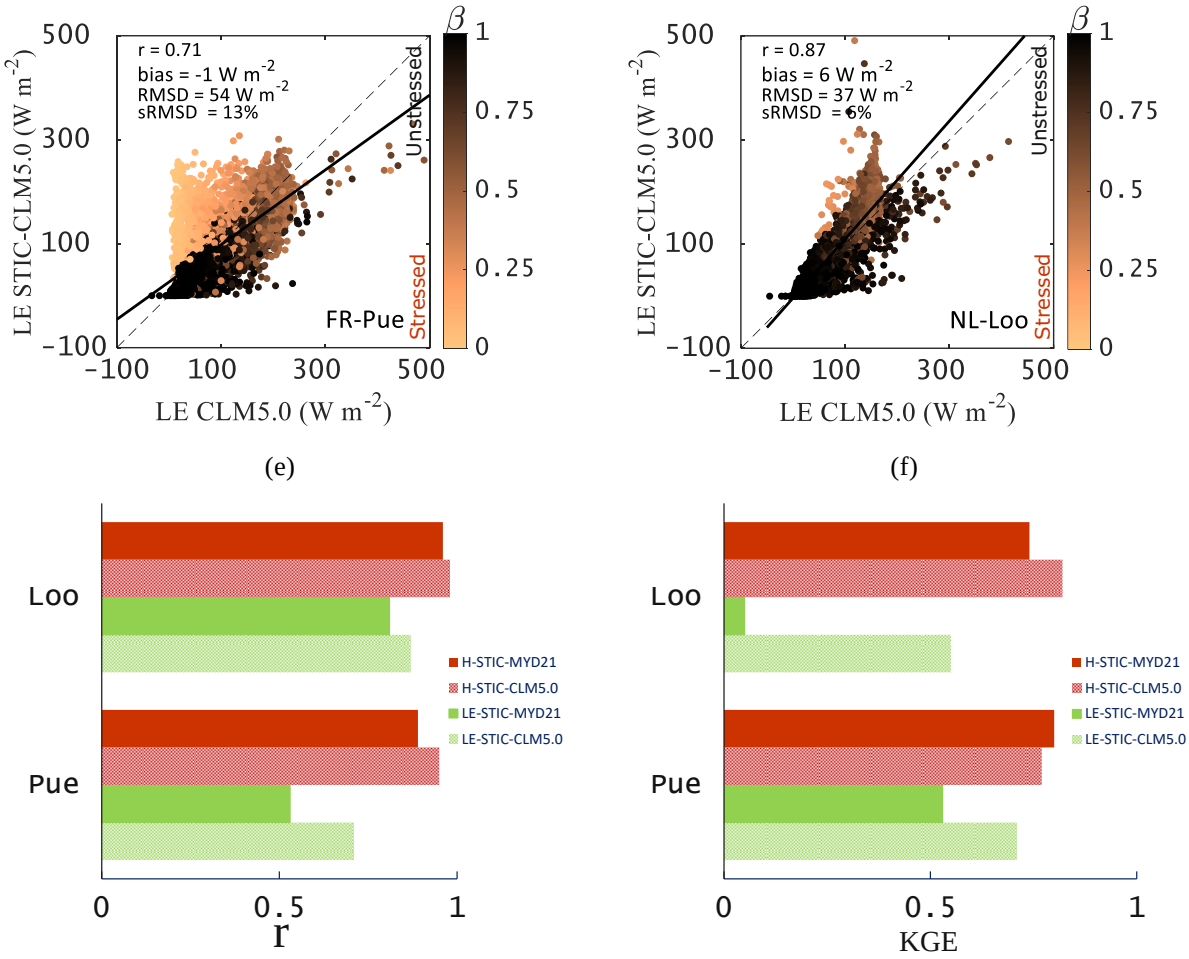

Figure 2. (a) – (b) Evaluation of CLM5.0 simulated LST with respect to MYD21 LST product in FR-Pue and NL-Loo for a range of CLM5.0 simulated beta factor (β); **(c) – (d)** Comparison between STIC1.2 simulated LE with respect to the virtual reality (scenario-1) for a range of CLM5.0 simulated beta factor (β); **(e) – (f)** Comparison of correlation and KGE statistics of LE and H between scenario-1 and scenario-2.

Like LST, comparison of surface energy balance fluxes between CLM5.0 and STIC1.2 was also made for the entire range of β. Comparison of LE between CLM5.0 and virtual reality STIC1.2 (STIC1.2-CLM5.0) (scenario-1) showed significant correlation between them (r = 0.71 – 0.86, $p<0.05$) in both the sites, with sRMSD and KGE of 6 – 13% and 0.55 – 0.71 (Figure 2c – d; Figure 2e – f). However, the correlation and KGE statistics of LE was degraded (r = 0.53 – 0.81; KGE: 0.05 – 0.53) when STIC1.2 was forced with MYD21 LST (STIC1.2-MYD21) (scenario-2). Interestingly, the two models showed stronger agreement for H as compared to LE in scenario-1 and scenario-2 in both the sites. In scenario-1, a significant correlation of 0.95 – 0.98 ($p<0.05$) (**Figure S1** in Supporting Information), sRMSD of 36 – 44%, and KGE 0.77 – 0.82 (Figure 2e – f) was found. Like LE, the correlation and KGE statistics of H also degraded (r = 0.89 – 0.96; KGE: 0.74 – 0.80) when STIC1.2 was forced with MYD21 LST (STIC1.2-MYD21) (scenario-2). There are two aspects in these results that are worth highlighting. It is evident that in scenario-1, the same LST conditions produced different LE and H in CLM5.0 and STIC1.2-CLM5.0. This is because CLM5.0 and STIC1.2-CLM5.0 formulate the water stress in

different ways. In STIC1.2, the water stress factor (I_{sm}) is calculated as an inverse of aggregated wetness of canopy-soil complex (Mallick et al., 2022, 2018), which controls the transition from potential to actual evaporation. This implies that $I_{sm} \rightarrow 1$ on the unstressed surface and $I_{sm} \rightarrow 0$ on the stressed surface. Therefore, I_{sm} is critical for providing a constraint against which the conductances are estimated. In STIC1.2-CLM5.0, the simulated LST from CLM5.0 is directly used for estimating I_{sm} in conjunction with air and dewpoint temperatures by exploiting the psychrometric theory of vapor pressure-temperature slope relationship (details in Mallick et al., 2022). In CLM5.0, the β-factor is estimated based on the simulated leaf water potential of the plant hydraulic system following a sigmoidal function accounting for the water potential at 50% loss of stomata conductance and a shape-fitting parameter (Kennedy et al., 2019). These two structurally different ways of formulating plant water stress tend to produce different water stress conditions in the two sites under the same LST. For a detailed investigation, a comparison between I_{sm} versus β is shown in the scatterplots in Supporting Information (**Figure S2a, b**). In FR-Pue, relatively less stressed conditions in STIC1.2 (i.e., $I_{sm} > \beta$) was evident with increasing LST (from 20 – 30 °C), part of which also coincided with high D_a (D_a >30 hPa) (datapoints above zero-line in **Figure S2** in the Supporting Information document). These conditions tend to produce an overestimation of LE in STIC1.2 in the scenario-1 despite it is virtually stressed (β<0.3). On the other side, relatively more stressed conditions in STIC1.2 (i.e., $I_{sm} < \beta$) for a wide range of D_a values was also visible at both sites (datapoints below zero-line in **Figure S2** in the Supporting Information). This is more evident in NL-Loo where β simulated by CLM5.0 is systematically larger (i.e., close to unstressed) than its counterpart in STIC1.2 (i.e., I_{sm}) for the entire range of LST values. In addition, the comparison of the simulated energy fluxes and the β factor across the two scenarios (i.e., CLM5.0 LST vs. MYD21 LST) and the two selected sites (i.e., FR-Pue vs. NL-Loo) allow to better assess the relative role of LST on SEB in the diagnostic and prognostic models. For example, in **Figure 2f**, LE at NL-Loo revealed distinct differences between STIC1.2-CLM5.0 and STIC1.2-MYD21. This is the site where consistent positive bias was found between CLM5.0 and MYD21 LST, however the relative difference in the water stress factor simulated by the two models does not drastically change between scenario-1 and scenario-2 (see **Figure S2c, d**).

Finally, it is also important to highlight that larger LE fluxes simulated by STIC1.2-CLM5.0 under soil and atmospheric drought conditions are associated with more stress conditions at the ecosystem scale. In addition to the water stress, the differences in stomatal and aerodynamic conductance formulation in the two models might also have produced different conductances values and the results are consequently reflected on the surface energy balance fluxes. While a cold (warm) LST bias during high water stress increases the likelihood possibility of unstressed (stressed) stomatal conductance simulation through STIC1.2, it simultaneously increases the possibility of a low (high) aerodynamic conductance simulation as well, ultimately leading to substantial differences in LE and H response to soil and atmospheric drought conditions. Thus, all these different aspects suggest a further analysis of the simulated biophysical conductances in both STIC1.2 and CLM5.0 to gain further insight on the explanation of the response of the two models to soil and atmospheric drought.

3.2 Biophysical conductances

The biophysical conductance (g_{cs}/g_a ratio) from STIC1.2-CLM5.0 appeared to be significantly correlated with CLM5.0 in FR-Pue ($r = 0.75$) across the entire range of β (scenario-1) (**Figure 3a**). However, profound differences in g_{cs}/g_a between STIC1.2-CLM5.0 and CLM5.0

was evident with rising soil and atmospheric drought (β: 0 – 0.25), which also corresponded with high magnitude of LST (>35°C) and D_a (>30 hPa) (**Figure 3a**). Similarly, the retrieved conductances from STIC1.2-MYD21 (scenario-2) also showed significant correlation (r = 0.68) yet marked difference with CLM5.0 (g_{cs}/g_a STIC1.2-MYD21 > g_{cs}/g_a CLM5.0) was evident (**Figure 3b**). In NL-Loo, analysis of the conductance ratio also revealed very similar pattern and substantial differences in the magnitude of g_{cs}/g_a between STIC1.2 and CLM5.0 for both the scenarios, with a relatively better correlation in scenario-1 (r = 0.63) as compared to scenario-2 (r = 0.54).

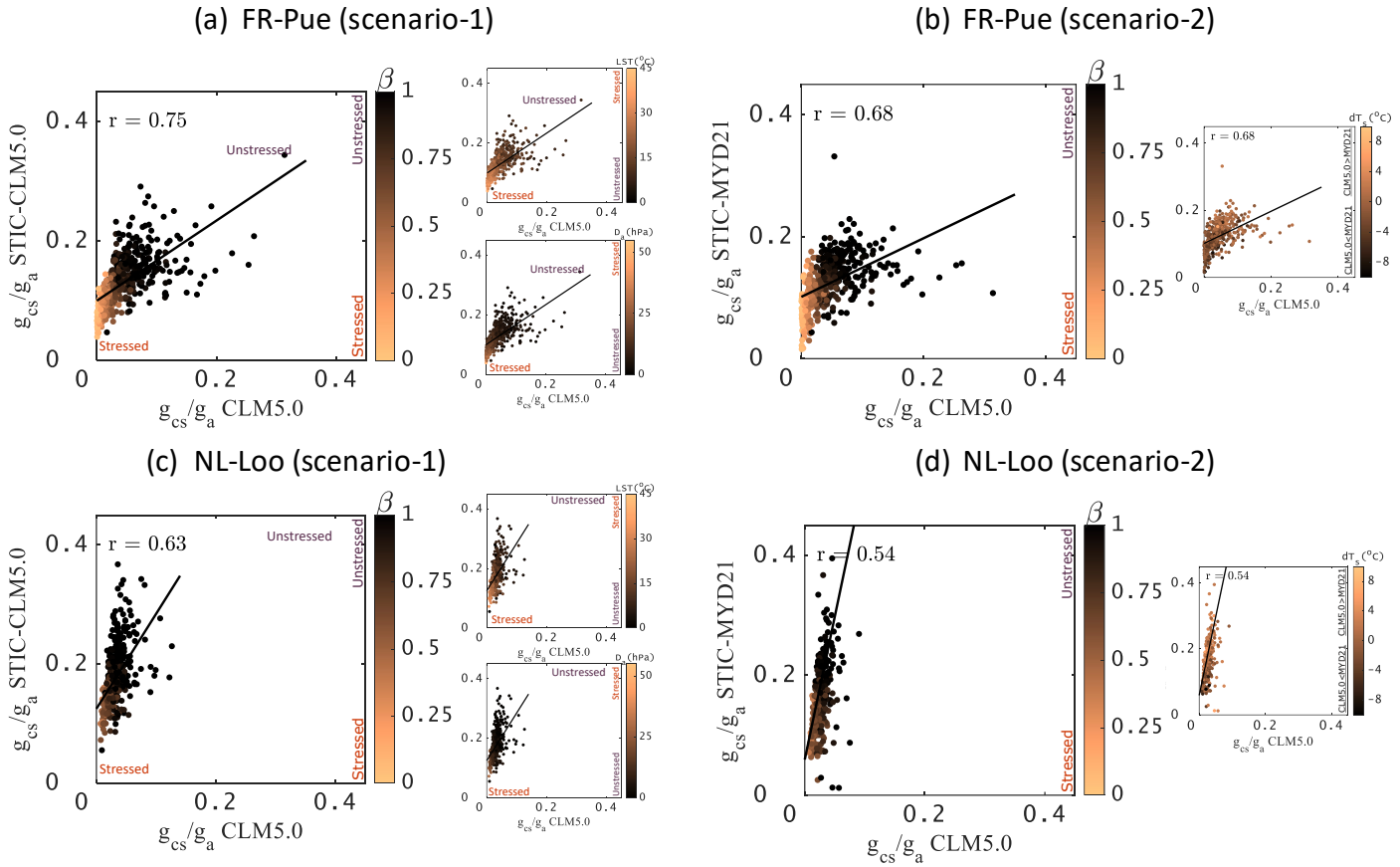

Figure 3. Scatterplots showing how the relationship and magnitude of the biophysical conductance ratios between STIC1.2 and CLM5.0 varies with different LST for a range of CLM5.0 water stress (β) in two different scenarios in FR-Pue (**a** and **b**) and NL-Loo (**c** and **d**).

Interestingly in both the sites, the difference in LST between CLM5.0 and MYD21 LST appeared to have small effects on differences in conductance ratios between CLM5.0 and STIC1.2. Some counter intuitive patterns also emerged out with respect to the behavior of g_{cs}/g_a with the coalition of soil and atmospheric drought (i.e., β) and LST. For example, in FR-Pue, CLM5.0 simulated colder LST as compared to MYD21 for LST>25°C, which is associated with high soil and atmospheric water stress in CLM5.0 (low β) (**Figure 2a, 3b**). Therefore, β from CLM5.0 is expected to be high (low water stress) and g_{cs}/g_a ratio from CLM5.0 is expected to show higher magnitude as compared to STIC1.2 in the scenario-2. This implies that although the conductances in CLM5.0 are sensitive to β simulation, both are somewhat less linked to the LST

simulation in the model. In a similar manner, despite predominantly low soil and atmospheric water stress in NL-Loo (β >0.60, LST: 10 – 15°C, D_a: 5 – 15 hPa), CLM5.0 showed very low g_{cs}/g_a ratio as compared to STIC1.2 (**Figure 3c**). This insensitivity in CLM5.0 is presumably generated by the loose coupling of surface energy balance to the plant hydraulics parameterization used in the model to calculate the stress factor.

To probe into the reasons on substantial differences in the conductance ratios between STIC1.2 and CLM5.0, and to understand the reasons for their different sensitivity to changes in LST, we further analyzed the response of the individual conductance components (g_{cs} and g_a) to soil and atmospheric drought proxies under scenario-1. Given stomatal conductance has a strong dependence on humidity deficit (Monteith, 1995), we used vapor pressure deficit to represent atmospheric drought proxy. Due to the strong connection of LST-air temperature difference (dT_{s-a}) with vegetation water stress and sensible heating (Anderson et al., 2007), we used dT_{s-a} to represent soil drought proxy (**Figure 4**).

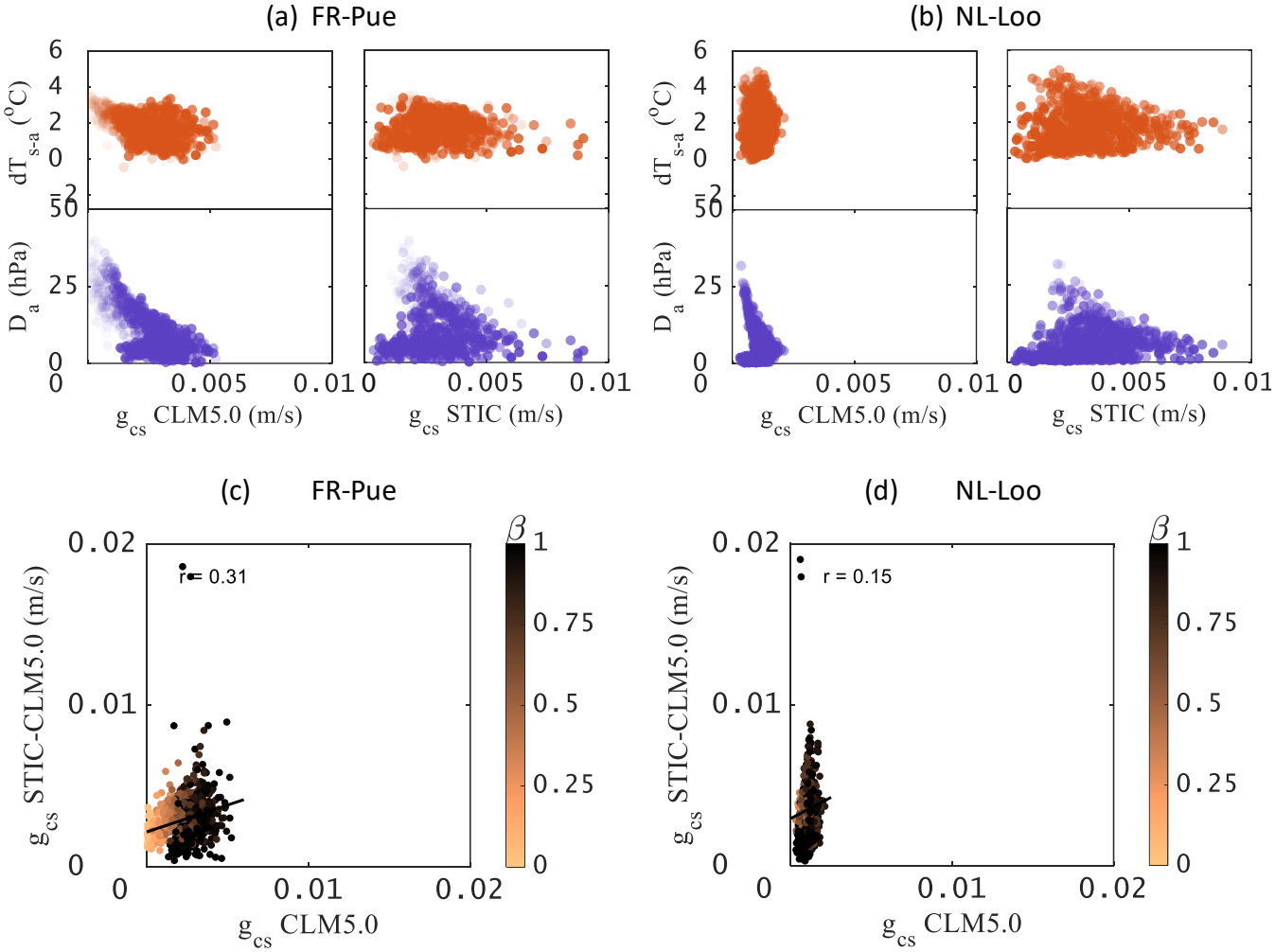

Figure 4. Response of retrieved g_{cs} to LST air temperature difference (dT_{s-a}) and atmospheric vapor pressure deficit (D_a) representing soil and atmospheric drought proxy, respectively, for (a) FR-Pue and (b) NL-Loo. Comparison between STIC1.2-derived g_{cs} and CLM5.0 g_{cs} for a broad spectrum of water stress simulated by CLM5.0.

In both FR-Pue and NL-Loo, CLM5.0 showed a non-linear reduction in g_{cs} with increasing D_a and reached an asymptotic decline afterwards (**Figure 4a – b**), which is a sign of a typical negative feedback. This control of atmospheric humidity deficit on stomatal action is subsequently modified by surface temperature feedback. A reduced transpiration due to partial stomatal closure can increase the surface temperature, which affects LST and the saturation vapor pressure at the vegetation surface. A negative temperature control loop is evident in FR-Pue where g_{cs} also declined with dT_{s-a}. However, no temperature control was found in NL-Loo, presumably due to mostly unstressed condition (high β) generated in CLM5.0. This unstressed condition is driven by a large soil water reservoir in NL-Loo reaching more than 30 m depth, in contrast with the soil depth of less than 1 m in FR-Pue. Finally, the narrow range of g_{cs} values simulated by CLM5.0 in NL-Loo, despite the favorable environmental conditions at the site compared to FR-Pue, is due to the stomatal conductance parameter value (i.e., g_1), which is by default equal to 2.35 for needleleaf evergreen temperate species (4.45 for broadleaf evergreen trees in FR-Pue). However, very surprisingly the magnitude of LE differed much less than as compared to g_{cs} between these two sites. For instance, in NL-Loo, CLM5 produced almost similar magnitude of LE as FR-Pue while having substantially lower g_{cs} as compared to FR-Pue. On the contrary, the scatterplot of g_{cs} versus D_a in STIC1.2 showed relatively complex pattern between atmospheric drought and g_{cs}, pointing towards feedback response (**Figure 4a – b**). Such type of feedback occurs when a change in evaporation causes a change in the conductance which subsequently affects the evaporation rate (Monteith, 1995). We found low g_{cs} in STIC1.2 at highest D_a because large humidity deficits strictly restrict water loss under high water stress. g_{cs} was also low at lowest D_a because of saturation and low humidity deficit. Conductance was optimum at intermediate D_a and evaporation. Due to the very different responses of g_{cs} to D_a in CLM5.0 and STIC1.2, the relationship between the two gcs was poor in both the sites and their absolute values also differed across the entire range of β (**Figure 4c – d**). This further emphasizes the fact that there is no universal function of stomatal conductance to atmospheric vapor pressure deficits and different ecosystems have different sensitivity of stomatal conductance to environmental variables. The similar principle also applies for the stomatal response function to soil drought.

Analysis of aerodynamic conductance (g_a) revealed very similar behavior of g_a with respect to the response of g_a to D_a and dT_{s-a} both in CLM5.0 and STIC1.2 (Figure 5a, 5b). In both the sites, a logarithmic response of g_a to D_a was evident in both the models, where g_a increased with increasing D_a and became asymptotic after D_a exceeded 25 hPa. The pattern of dT_{s-a} versus g_a was linear to exponential in both the models. However, marked differences in the magnitude of g_a between CLM5.0 and STIC1.2 was found in FR-Pue, although significantly high correlation between the two g_a estimates was found in both the sites ($r = 0.75 – 0.80$). The differences in absolute magnitude of g_a between the two models is presumably due to the differences in the model structure. While g_a estimation in CLM5.0 is based on the Monin-Obukhov Similarity Theory involving corrections due to atmospheric stability, parameterization of surface roughness lengths, estimation of g_a in STIC1.2 is based on LST and environmental variables without involving any atmospheric sub-models. However, the significant correlation between the two g_a estimates and their responses to soil/atmospheric drought metrics signifies the need of unified and common approach of aerodynamic conductances in both prognostic and diagnostic models to understand the differences in surface energy balance flux prediction. A possible solution to address this challenge could be the implementation of data-driven techniques

for the calculation of both g_a and g_{cs} (e.g., ElGhawi et al., 2023) in both prognostic and diagnostic approaches for modelling evapotranspiration.

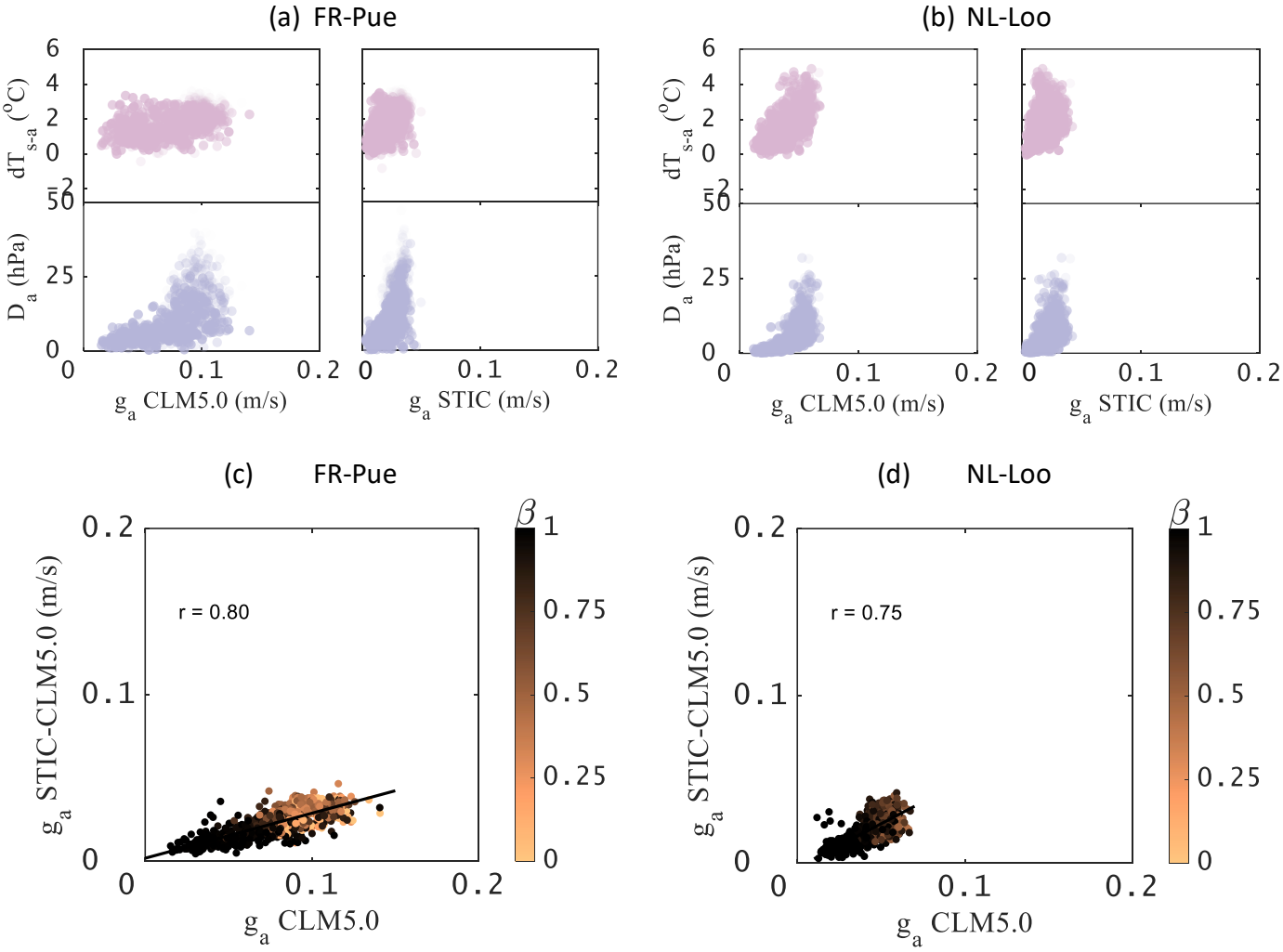

Figure 5. Response of retrieved g_a to LST air temperature difference (dT_{s-a}) and atmospheric vapor pressure deficit (D_a) representing soil and atmospheric drought proxy, respectively, for (a) FR-Pue and (b) NL-Loo. Comparison between STIC1.2-derived g_a and CLM5.0 g_a for a broad spectrum of water stress simulated by CLM5.0 for (c) FR-Pue and (d) NL-Loo.

3.3 Factor controlling conductances and fluxes in the models

To substantiate our findings from the previous sections, we further investigated the relationship of the individual conductances and surface energy balance fluxes as final model output with a host of environmental and surface variables by performing a partial least square regression (PLSR) analysis for the scenario-1 (**Figure 6**). If the Variable Importance in Projection (VIP) score exceeds a value of 0.8, the variable is considered to play an important role in determining the magnitude and variability on g_a, g_{cs}, LE and H, respectively (Trebs et al., 2021).

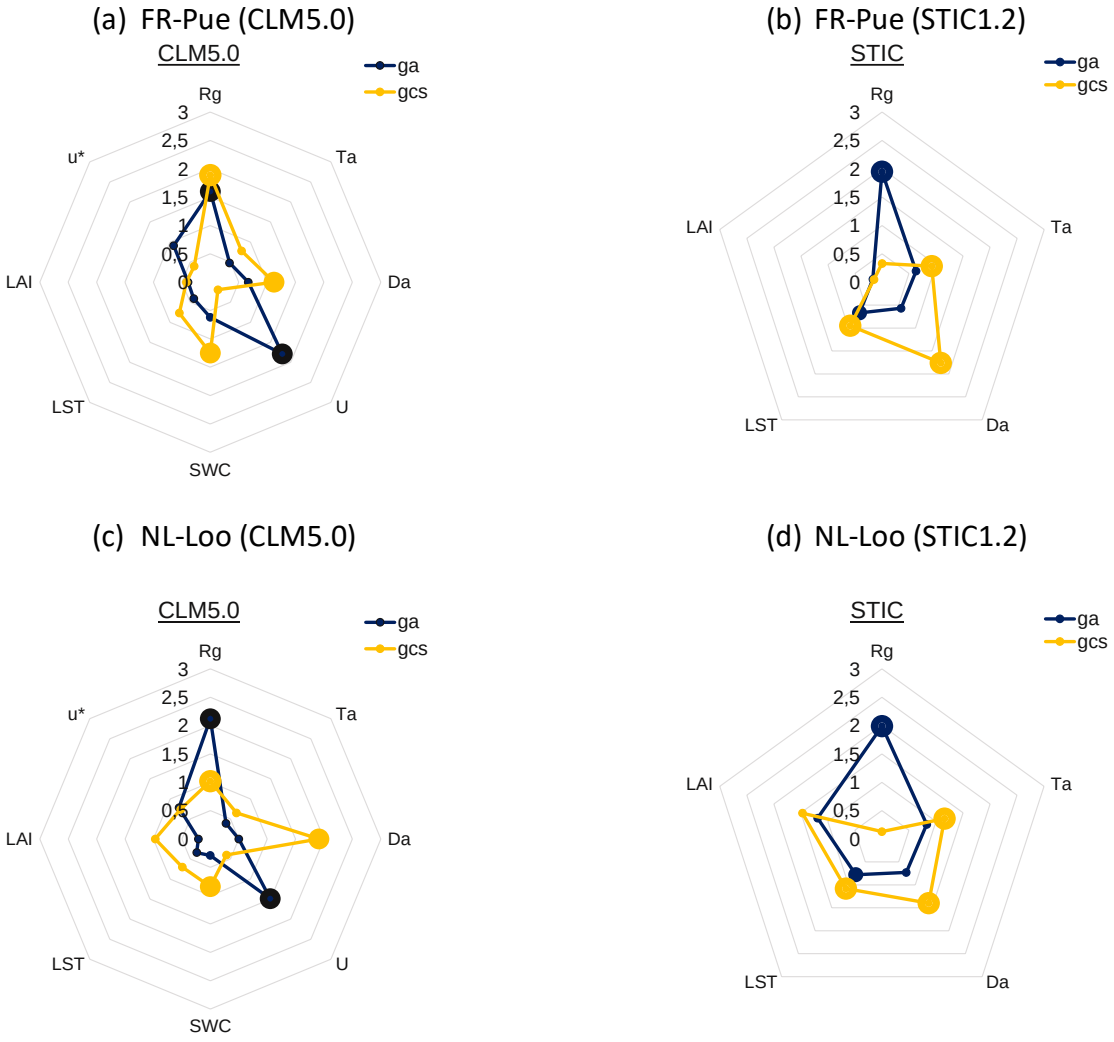

Figure 6. Radar charts of the Variable Importance in Projection (VIP) scores for aerodynamic and canopy-stomatal conductance (g_a and g_{cs}) estimated from CLM5.0 and STIC1.2 with respect to environmental, hydrological and land surface variables for both FR-Pue and NL-Loo. Here R_g is the shortwave radiation, T_a is the air temperature, D_a is the atmospheric vapor pressure deficit, U is the wind speed, SWC is the soil water content, LST is the land surface temperature, LAI is the leaf area index, and u^* is the friction velocity, respectively.

The results from the PLSR analysis indicated that for CLM5.0, while the shortwave radiation (R_g) and wind speed (U) has a major impact on the aerodynamic conductance, the g_{cs} is mainly regulated by R_g, D_a and simulated soil water content (SWC) in both the sites. Whereas for STIC1.2, while the effects of R_g and LST was maximum on g_a, the variations in g_{cs} were maximally impacted by LST, D_a and air temperature (T_a), respectively. The influence of R_g on the modeled g_{cs} in STIC1.2 apparently had minor importance. This could be due the fact that the effects of R_g is already accounted in the air temperature signal and no additional effects of R_g was noted. On the other hand, the large influence of R_g to g_{cs} in CLM5.0 could presumably be explained by the coupled photosynthesis-stomata conductance model where photosynthetically active radiation is directly used to solve the system of equations for sunlit and shaded leaves.

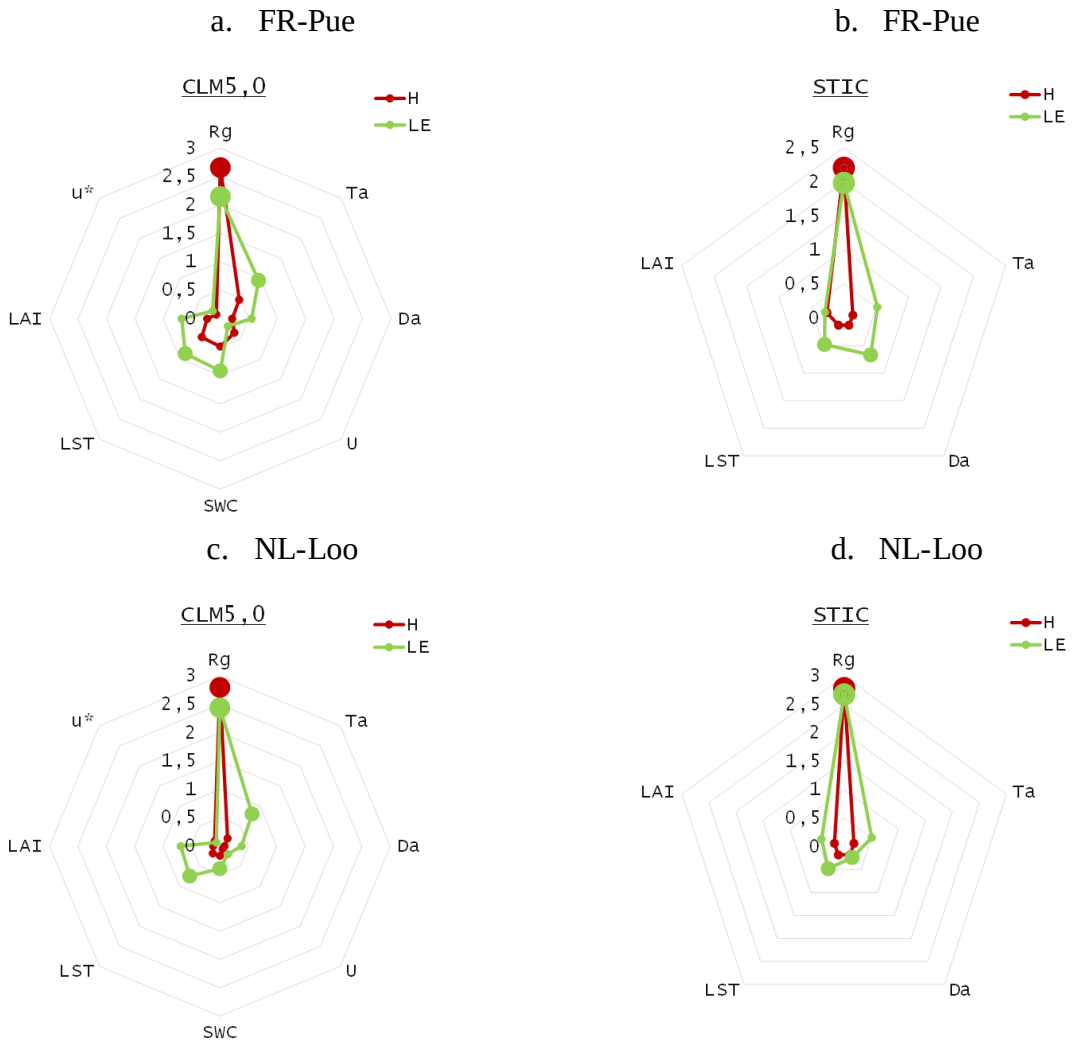

Figure 7. Radar charts of the Variable Importance in Projection (VIP) scores for latent and sensible heat fluxes (LE and H) estimated from CLM5.0 and STIC1.2 with respect to environmental, hydrological and land surface variables for both FR-Pue and NL-Loo. Here R_g is the shortwave radiation, T_a is the air temperature, D_a is the atmospheric vapor pressure deficit, U is the wind speed, SWC is the soil water content, LST is the land surface temperature, LAI is the leaf area index, and u^* is the friction velocity, respectively.

Another interesting feature emerging from the VIP analysis is the relatively stable importance of D_a in STIC1.2 to explain g_{cs} response across the two sites. In CLM5.0, the importance of D_a clearly increases in NL-Loo due to the marginal role played by SWC due to continuous supply of plant available water in this ecosystem. Finally, both STIC1.2 and CLM5.0 show an increasing importance of LAI to explain g_{cs} when moving from broadleaf evergreen trees (i.e., FR-Pue) to needleleaf evergreen trees (i.e., NL-Loo).

Similar analysis with the surface energy balance fluxes indicated that for CLM5.0, while R_g has the major impact on the sensible heat flux; R_g, T_a, SWC, and simulated LST was found to

have substantial control on the variability in LE in both the sites. For STIC1.2, despite the same pattern was found for sensible heat flux, however, the variability of LE was significantly controlled by R_g, D_a, and LST. It is also worth mentioning that the effects of the environmental variables were substantially stronger on the conductances as compared to the surface energy balance fluxes. This PLSR analysis further emphasizes the fact that for using model and satellite-based evaporation as a water cycle predictor, we not only need to capture the magnitude and variability of the biophysical conductances, but we need consensus models that will explain the effects of complex coalition of soil and atmospheric drought on the conductances. However, this is a non-trivial problem and too often such complexities are tackled with over simplified or over-parameterized models involving too many calibrations that do not consider the interactions and feedbacks (whether negative or feedforward) that are observed in nature.

5 Conclusions and Future Implications

The study critically evaluates the evaporation response and the inherent biophysical conductances, namely stomatal and aerodynamic, simulated by a diagnostic non-parametric thermal remote sensing model (i.e., STIC1.2) and by a prognostic state-of-the-art land surface model (i.e., CLM5.0). We implemented a virtual reality experimental framework to understand the conjugate effects of soil and atmospheric drought on the response of these two conductances that have significant impact in modulating evaporation. In this framework, the two models share the same upper (i.e., atmospheric) and lower (i.e., land surface temperature) boundary conditions. An extended analysis on the comparison of the conductances and fluxes based on soil-atmospheric water stress factor led us to the following conclusion and the emergent future implications:

a) Despite the relatively good agreement in the simulated surface energy balance fluxes, the two models show substantial divergence in reproducing the magnitude and variability of the aerodynamic and stomatal conductances. This divergence is explained by the structural differences in the formulation of plant water stress in two different models, which tend to produce very different water stress conditions in two contrasting forest sites despite the two models had the same land surface temperature and vapor pressure deficit conditions.
b) Analysis of the individual biophysical conductances revealed that the profound differences in the magnitude and response of stomatal and aerodynamic conductance was not only associated with the water stress factor, but also due to different functional representation of the individual conductances in two different models. The differences in the functional representation led to very different response of the aerodynamic and stomatal conductances to soil and atmospheric drought in the models.
c) The magnitude and variability of the aerodynamic conductance of CLM5.0 is largely explained by wind speed and solar radiation across the two selected sites, while in STIC1.2 it is mainly influenced by solar radiation and a larger host of variables including D_a, LST, and T_a. On the other hand, the magnitude and variability of stomatal conductance is explained by solar radiation, D_a, and soil water content in CLM5.0, and by D_a, T_a, and LST in STIC1.2.
d) The substantial differences in water stress estimation and in the biophysical conductances led to differences in evaporative flux estimates of CLM5.0 and STIC1.2. These differences are larger for LE and for the more humid site of NL-Loo.

Our study results have important implications for both the remote sensing and the land surface community, highlighting the need for an in-depth comparison of different modelling approaches to understand their biases and uncertainty. More specifically, the findings of our work suggest the need of a unified approach in the treatment of the biophysical conductances with respect to their responses to water stress in the two very diverse modelling community for achieving a more robust multi-model assessment of the evaporation fluxes.

Acknowledgments

This work was supported by the Luxembourg National Research Fund (FNR) CORE program (C19/SR/13652816/CAPACITY). KM also acknowledges the financial support of the FNR INTER MOBILITY program (INTER/MOBILITY/2020/14521920/MONASTIC). TH was supported by the European ECOSTRESS Hub project (EEH, Contract No. 4000129873/20/I-NS), funded by the European Space Agency (ESA).

Open Research

The FLUXNET data used for atmospheric forcing in the study are available at https://fluxnet.org/data/fluxnet2015-dataset. CLM5.0 is publicly available through the Community Terrestrial System Model (CTSM) git repository (Tag name: release-clm5.0.30) via https://github.com/ESCOMP/ctsm (CTSM, 2017/2022). The results of the numerical experiments and Matlab scripts used for the data analysis of this manuscript are available at ZENODO repository via https://doi.org/10.5281/zenodo.8318671.

References

Anderson, M. C., Norman, J. M., Mecikalski, J. R., Otkin, J. A., & Kustas, W. P. (2007). A climatological study of evapotranspiration and moisture stress across the continental United States based on thermal remote sensing: 2. Surface moisture climatology. *Journal of Geophysical Research: Atmospheres*, 112(D11). https://doi.org/10.1029/2006JD007507

Anderson, M., Kustas, W., Alfieri, J., Gao, F., Hain, C., Prueger, J., Evett, S., Colaizzi, P., Howell, T. & Chávez, J. (2012). Mapping daily evapotranspiration at Landsat spatial scales during the BEAREX'08 field campaign. *Advances in Water Resources.* 50, 162 – 177, https://doi.org/10.1016/j.advwatres.2012.06.005

Bhattarai, N., Mallick, K., Brunsell, N. A., Sun, G., & Jain, M. (2018). Regional evapotranspiration from an image-based implementation of the Surface Temperature Initiated Closure (STIC1. 2) model and its validation across an aridity gradient in the conterminous US. *Hydrology and Earth System Sciences*, 22(4), 2311-2341. https://doi.org/10.5194/hess-22-2311-2018

Bhattarai, N., Mallick, K., Stuart, J., Vishwakarma, B. D., Niraula, R., Sen, S., & Jain, M. (2019). An automated multi-model evapotranspiration mapping framework using remotely sensed and reanalysis data. *Remote Sensing of Environment*, 229, 69-92. https://doi.org/10.1016/j.rse.2019.04.026

Beck, H. E., Zimmermann, N. E., McVicar, T. R., Vergopolan, N., Berg, A., & Wood, E. F. (2018). Present and future Köppen-Geiger climate classification maps at 1-km resolution, *Scientific data*, 5, 1–12. https://doi.org/10.1038/sdata.2018.214

Byrne, M. P., & O'Gorman, P. A. (2013). Link between land-ocean warming contrast and surface relative humidities in simulations with coupled climate models. *Geophysical Research Letters*, 40(19), 5223-5227. https://doi.org/10.1002/grl.50971

Chen, Y., K. Yang, D., Zhou, Qin, J., & Guo, X. (2010). Improving the Noah land surface model in arid regions with an appropriate parameterization of the thermal roughness length. *Journal of Hydrometeorology*, 11(4), 995–1006. https://doi.org/10.1175/2010JHM1185.1

Chen, L., Dirmeyer, P.A. (2020). Reconciling the disagreement between observed and simulated temperature responses to deforestation. *Nature Communications*. 11(1), 202. https://doi.org/10.1038/s41467-019-14017-0

Cabon, A., Mouillot, F., Lempereur, M., Ourcival, J.-M., Simioni, G., & Limousin, J.-M. (2018). Thinning increases tree growth by delaying drought-induced growth cessation in a Mediterranean evergreen oak coppice. *Forest Ecology and Management*, 409, 333-342. https://doi.org/10.1016/j.foreco.2017.11.030

Damour, G., Simonneau, T., Cochard, H., & Urban, L. (2010). An overview of models of stomatal conductance at the leaf level. *Plant, cell & environment*, 33(9), 1419-1438. https://doi.org/10.1111/j.1365-3040.2010.02181.x

de Jong, S. (1993). SIMPLS: an alternative approach to partial least squares regression. *Chemometrics and Intelligent Laboratory Systems*, 18(3), 251-263. https://doi.org/10.1016/0169-7439(93)85002-X

ElGhawi, R., Kraft, B., Reimers, C., Reichstein, M., Körner, M., Gentine, P., & Winkler, A. J. (2023). Hybrid modeling of evapotranspiration: inferring stomatal and aerodynamic resistances using combined physics-based and machine learning. *Environmental Research Letters*, 18(3). https://doi.org/10.1088/1748-9326/acbbe0

Gao, Z., N. Chae, J., Kim, J., Hong, T. Choi, & Lee H. (2004). Modeling of surface energy partitioning, surface temperature, and soil wetness in the Tibetan prairie using the Simple Biosphere Model 2 (SiB2). *Journal of Geophysical Research: Atmosphetres* 109, D06102, https://doi.org/10.1029/2003JD004089

Gevaert, A. I., Miralles, D. G., de Jeu, R. A., Schellekens, J., & Dolman, A. J. (2018). Soil moisture-temperature coupling in a set of land surface models. *Journal of Geophysical Research: Atmospheres*, 123(3), 1481–1498. https://doi.org/10.1002/2017JD027346

Gupta, H. V., Kling, H., Yilmaz, K. K., & Martinez, G. F. (2009). Decomposition of the mean squared error and NSE performance criteria: Implications for improving hydrological modelling. *Journal of hydrology*, 377(1-2), 80-91. https://doi.org/10.1016/j.jhydrol.2009.08.003

Green, J. K., Ballantyne, A., Abramoff, R., Gentine, P., Makowski, D., & Ciais, P. (2022). Surface temperatures reveal the patterns of vegetation water stress and their environmental drivers across the tropical Americas. *Global Change Biology*, 28(9), 2940– 2955. https://doi.org/10.1111/gcb.16139

Holwerda, F., Bruijnzeel, L. A., Scatena, F. N., Vugts, H. F., & Meesters A.G.C.A. (2012). Wet canopy evaporation from a Puerto Rican lower montane rain forest: The importance of realistically estimated aerodynamic conductance. *Journal of Hydrology*, 11, 414-415, https://doi.org/10.1016/j.hydrol.2011.07.033

Kennedy, D., Swenson, S., Oleson, K. W., Lawrence, D. M., Fisher, R., da Costa, A. C. L., & Gentine, P. (2019). Implementing plant hydraulics in the Community Land Model, Version 5. *Journal of Advances in Modeling Earth Systems*,11(2), 485–513. https://doi.org/10.1029/2018ms001500

Koch, J., Siemann, A., Stisen, S., & Sheffield, J. (2016). Spatial validation of large-scale land surface models against monthly land surface temperature patterns using innovative performance metrics. *Journal of Geophysical Research: Atmospheres*, 121(10), 5430– 5452, https://doi.org/10.1002/2015JD024482

Koster, R.D., Dirmeyer, P.A., Guo, Z., Bonan, G., Chan, E., Cox, P., Gordon, C.T., Kanae, S., Kowalczyk, E., Lawrence, D., Liu, P., Lu, C-H., Malyshev, S., McAvaney, B., Mitchell, K., Mocko, D., Oki, T., Oleson, K., Pitman, A., Sud, Y.C., Taylor, C.M., Verseghy, D., Vasic, R., Xue, Y., & Yamada, T. (2004). Regions of strong coupling between soil moisture and precipitation. *Science*, 305(5687), 1138–1140. https://doi.org/10.1126/science.1100217

Koster, R. D., Sud, Y. C. , Guo, Z., Dirmeyer, P. A., Bonan, G., Oleson, K. W., Chan, E., Verseghy, D., Cox, P., Davies, H., Kowalczyk, E., Gordon, C. T. , Kanae, S., Lawrence, D., Liu, P., Mocko, D., Lu, C., Mitchell, K., Malyshev, S., McAvaney, B., Oki, T., Yamada, T., Pitman, A., Taylor, C. M., Vasic, R., & Xue, Y. (2006). GLACE: The Global Land–Atmosphere Coupling Experiment. Part I: Overview. *Journal of Hydrometeorology*, 7(4), 590-610. https://doi.org/10.1175/JHM510.1

Kustas, W., & Anderson, M. (2009). Advances in thermal infrared remote sensing for land surface modeling. *Agricultural and Forest Meteorology*, 149(12), 2071-2081. https://doi.org/10.1016/j.agrformet.2009.05.016

Kustas, W. P., Nieto, H., Morillas, L., Anderson, M. C., Alfieri, J. G., Hipps, L. E., Villagarcia, L., Domingo, F., & Garcia, M. (2016). Revisiting the paper "Using radiometric surface temperature for surface energy flux estimation in Mediterranean drylands from a two-source perspective". *Remote Sensing of Environment*, 184, 645-653. https://doi.org/10.1016/j.rse.2016.07.024

Lawrence, D., Fisher, R., Koven, C., Oleson, K., Swenson, S., Vertenstein, M., Andre, B., Bonan, G., Ghimire, B., & van Kampenhout, L. (2018). Technical description of version 5.0 of the Community Land Model (CLM), Natl. Cent. Atmospheric Res. (NCAR), https://www.cesm.ucar.edu/models/cesm2/land/ CLM50_Tech_Note.pdf 2018

Lawrence, D. M., Fisher, R. A., Koven, C. D., Oleson, K. W., Swenson, S. C., Bonan, G., Collier, N., Ghimire, B., van Kampenhout, L., Kennedy, D., Kluzek, E., Lawrence, P. J., Li, F., Li, H., Lombardozzi, D., Riley, W. J., Sacks, W. J., Shi, M., Vertenstein, M., Wieder, W. R., Xu, C., Ali, A. A., Badger, A. M., Bisht, G., van den Broeke, M., Brunke, M. A., Burns, S. P., Buzan, J., Clark, M., Craig, A., Dahlin, K., Drewniak, B., Fisher, J. B., Flanner, M., Fox, A. M., Gentine, P., Hoffman, F., Keppel-Aleks, G., Knox, R., Kumar, S., Lenaerts, J., Leung, L. R., Lipscomb, W. H., Lu, Y., Pandey, A., Pelletier, J. D., Perket, J., Randerson, J. T., Ricciuto, D. M., Sanderson, B. M., Slater, A., Subin, Z. M., Tang, J., Thomas, R. Q., Val Martin, M., & Zeng, X. (2019). The Community Land Model version 5: Description of new features, benchmarking, and impact of forcing uncertainty. *Journal of Advances in Modeling Earth Systems*, 11, 4245–4287. https://doi.org/10.1029/2018MS001583

Levine, P. A., Randerson, J. T., Swenson, S. C., & Lawrence, D. M. (2016). Evaluating the strength of the land–atmosphere moisture feedback in Earth system models using satellite observations. *Hydrology and Earth System Sciences*, 20(12), 4837-4856. https://doi.org/10.5194/hess-20-4837-2016

Liao, W., Liu, X., Burakowski, E., Wang, D., Wang, L., & Li, D. (2020). Sensitivities and responses of land surface temperature to deforestation-induced biophysical changes in two global earth system models. *Journal of Climate*, 33(19), 8381-8399. https://doi.org/10.1175/JCLI-D-19-0725.1

Long, D., Longuevergne, L., & Scanlon, B. R. (2014). Uncertainty in evapotranspiration from land surface modeling, remote sensing, and GRACE satellites. *Water Resources Research*, 50(2), 1131-1151. https://doi.org/10.1002/2013WR014581.

Long, D., Yan, L., Bai, L., Zhang, C., Li, X., Lei, H., Yang, H., Tian, F., Zeng, C., Meng, X. & Shi, C. (2020). Generation of MODIS-like land surface temperatures under all-weather conditions based on a data fusion approach. *Remote Sensing of Environment*, 246, 111863. https://doi.org/10.1016/j.rse.2020.111863

Ma, X., Jin, J., Zhu, L., & Liu, J. (2021). Evaluating and improving simulations of diurnal variation in land surface temperature with the Community Land Model for the Tibetan Plateau. *PeerJ*, 9, e11040. https://doi.org/10.7717/peerj.11040

Mallick, K., Toivonen, E., Trebs, I., Boegh, E., Cleverly, J., Eamus, D., Koivusalo, H., Drewry, D., Arndt, S.K., Griebel, A. & Beringer, J. (2018). Bridging Thermal Infrared Sensing and Physically-Based Evapotranspiration Modeling: From Theoretical Implementation to Validation Across an Aridity Gradient in Australian Ecosystems. *Water Resources Research*, 54(5), 3409-3435. https://doi.org/10.1029/2017wr021357

Mallick, K., Trebs, I., Boegh, E., Giustarini, L., Schlerf, M., Drewry, D.T., Hoffmann, L., Von Randow, C., Kruijt, B., Araùjo, A. & Saleska, S. (2016). Canopy-scale biophysical controls of transpiration and evaporation in the Amazon Basin. *Hydrology and Earth System Sciences*, 20(10), 4237-4264. https://doi.org/10.5194/hess-20-4237-2016.

Mallick, K., Baldocchi, D., Jarvis, A., Hu, T., Trebs, I., Sulis, M., Bhattarai, N., Bossung, C., Eid, Y., Cleverly, J. & Beringer, J. (2022). Insights Into the Aerodynamic Versus Radiometric Surface Temperature Debate in Thermal-Based Evaporation Modeling. *Geophysical Research Letters*, 49(15), e2021GL097568. https://doi.org/10.1029/2021GL097568

Massmann, A., Gentine, P., and Lin, C. (2019). When does vapor pressure deficit drive or reduce evapotranspiration? *Journal of Advances in Modeling Earth Systems*, 11, 3305–3320. https://doi.org/10.1029/2019MS001790

Medlyn, B.E., Duursma, R.A., Eamus, D., Ellsworth, D.S., Prentice, I.C., Barton, C.V.M., Crous, K.Y., De Angelis, P., Freeman, M., & Wingate, L. (2011). Reconciling the optimal and empirical approaches to modelling stomatal conductance. *Global Change Biology*, 17: 2134–2144. https://doi.org/10.1111/j.1365-2486.2010.02375.x

Mitchell, K.E., Lohmann, D., Houser, P.R., Wood, E.F., Schaake, J.C., Robock, A., Cosgrove, B.A., Sheffield, J., Duan, Q., Luo, L. and Higgins, R.W. (2004). The multi-institution North American Land Data Assimilation System (NLDAS): Utilizing multiple GCIP products and partners in a continental distributed hydrological modeling system. *Journal of Geophysical Research*: Atmospheres, 109(D7). https://doi.org/10.1029/2003JD003823.

Meier, R., Davin, E. L., Bonan, G. B., Lawrence, D. M., Hu, X., Duveiller, G., Prigent, C., & Seneviratne, S. I. (2022). Impacts of a revised surface roughness parameterization in the Community Land Model 5.1. *Geoscientific Model Development*, 15, 2365–2393, https://doi.org/10.5194/gmd-15-2365-2022

Monteith, J. L. (1965). Evaporation and environment. In Symposia of the society for experimental biology (Vol. 19, pp. 205-234). Cambridge University Press (CUP) Cambridge. https://repository.rothamsted.ac.uk/item/8v5v7/evaporation-and-environment

Monteith, J. L. (1995). Accommodation between transpiring vegetation and the convective boundary layer. *Journal of Hydrology*, 166(3-4), 251-263. https://doi.org/10.1016/0022-1694(94)05086-D

Morrow, N., & Friedl, M.A. (1998). Modeling biophysical controls on land surface temperature reflectance in grasslands. *Agricultural and Forest Meteorology*, 92(3), 147-161. https://doi.org/10.1016/S0168-1923(98)00098-7

Mott, K. A. (2007). Leaf hydraulic conductivity and stomatal responses to humidity in amphistomatous leaves. *Plant, Cell & Environment*, 30(11), 1444-1449. https://doi.org/10.1111/j.1365-3040.2007.01720.x

Pastorello, G., Trotta, C., Canfora, E., Chu, H., Christianson, D., Cheah, Y.W., Poindexter, C., Chen, J., Elbashandy, A., Humphrey, M. and Isaac, P. (2020), The FLUXNET2015 dataset and the ONEFlux processing pipeline for eddy covariance data. *Scientific Data* 7, 225, https://doi.org/10.1038/s41597-020-534-3

Penman, H. L. (1948). Natural evaporation from open water, bare soil and grass. Proceedings of the Royal Society of London. Series A. *Mathematical and Physical Sciences*, 193(1032), 120-145. https://doi.org/10.1098/rspa.1948.0037

Reichstein, M., Tenhunen, J. D., Roupsard, O., Ourcival, J.-M., Rambal, S., Dore, S., & Valentini, R. (2002). Ecosystem respiration in two Mediterranean evergreen Holm Oak forests: drought effects and decomposition dynamics. *Functional Ecology*, 16, 27–39, https://doi.org/10.1046/j.0269-8463.2001.00597.x

Sellers, P. J., Mintz, Y., Sud, Y. C., & Dalcher, A. (1986). A Simple Biosphere Model (SIB) for Use within General Circulation Models. *Journal of Atmospheric Sciences*, 43(6), 505-531. https://doi.org/10.1175/1520-0469(1986)043<0505:ASBMFU>2.0.CO;2

Siemann, A. L., Coccia, G., Pan, M., & Wood, E. F. (2016) Development and analysis of a long term, global, terrestrial land surface temperature dataset based on HIRS satellite retrievals. *Journal of Climate*, 29(10), 3589– 3606. https://doi.org/10.1175/JCLI-D-15-0378.1

Thakur, G., Schymanski, S. J., Mallick, K., Trebs, I., & Sulis, M. (2022). Downwelling longwave radiation and sensible heat flux observations are critical for surface temperature and emissivity estimation from flux tower data. *Scientific Reports*, 12(1), 8592. https://doi.org/10.1038/s41598-022-12304-3

Tiktak, A., & Bouten, W. (1994), Soil water dynamics and long-term water balances of a Douglas fir stand in the Netherlands. *Journal of Hydrology*, 156(1-4), 265-283. https://doi.org/10.1016/0022-1694(94)90081-7

Trebs, I., Mallick, K., Bhattarai, N., Sulis, M., Cleverly, J., Woodgate, W., Silberstein, R., Hinko-Najera, N., Beringer, J., Meyer, W.S. and Su, Z. (2021). The role of aerodynamic resistance in thermal remote sensing-based evapotranspiration models. *Remote Sensing of Environment*, 264, 112602. https://doi.org/10.1016/j.rse.2021.112602

Trigo, I. F., Boussetta, S., Viterbo, P., Balsamo, G., Beljaars, A., & Sandu., I. (2015). Comparison of model land skin temperature with remotely sensed estimates and assessment of surface-atmosphere coupling. *Journal of Geophysical Research: Atmospheres*. 120(23), 12,096–12,111. https://doi.org/10.1002/2015JD023812

Ukkola, A. M., Haughton, N., De Kauwe, M. G., Abramowitz, G., & Pitman, A. J. (2017). FluxnetLSM R package (v1.0): A community tool for processing FLUXNET data for use in land surface modelling. *Geoscientific Model Development*, 10, 3379–3390, https://doi.org/10.5194/gmd-10-3379-2017

Wang, A., M. Barlage, X. Zeng, & C. S. Draper (2014), Comparison of land skin temperature from a land model, remote sensing and in situ measurement. *Journal of Geophysical Research: Atmospheres*, 119, 3093–3106, https://doi.org/10.1002/2013JD021026.

Wang, S., Pan, M., Mu, Q., Shi, X., Mao, J., Brümmer, C., Jassal, R.S., Krishnan, P., Li, J. and Black, T.A. (2015). Comparing evapotranspiration from Eddy covariance measurements, water budgets, remote sensing, and land surface models over Canada. *Journal of Hydrometeorology*, 16(4), 1540–1560. https://doi.org/10.1175/Jhm-D-14-0189.1

Yuan, X., Hamdi, R., Ochege, F. U., De Maeyer, P., Kurban, A., & Chen, X. (2021). Assessment of surface roughness and fractional vegetation coverage in the CoLM for modeling regional land surface temperature. *Agricultural and Forest Meteorology*, 303, 108390. https://doi.org/10.1016/j.agrformet.2021.108390

Zeng, X., Wang, Z., & Wang, A. (2012). Surface skin temperature and the interplay between sensible and ground heat fluxes over arid regions. *Journal of Hydrometeorology*, 13(4), 1359-1370. https://doi.org/10.1175/JHM-D-11-0117.1.

Zhang, B., Xia, Y., Long, B., Hobbins, M., Zhao, X., Hain, C., Li, Y., & Anderson, M.C. (2020). Evaluation and comparison of multiple evapotranspiration data models over the contiguous United States: Implications for the next phase of NLDAS (NLDAS-Testbed) development. *Agricultural and Forest Meteorology*. 280, 107810. https://doi.org/10.1016/j.agrformet.2019.107810

Zhang, X., Zhou, J., Liang, S., & Wang, D. (2021), A practical reanalysis data and thermal infrared remote sensing data merging (RTM) method for reconstruction of a 1-km all-weather land surface temperature. *Remote Sensing of Environment*, 260, 112437. https://doi.org/10.1016/j.rse.2021.112437

Zheng, W., Wei, H., Wang, Z., Zeng, X., Meng, J., Ek, M., & Derber, J. (2012). Improvement of daytime land surface skin temperature overarid regions in the NCEP GFS model and its impact on satellite data assimilation, *Journal of Geophysical Research*, 117(D6), D06117, https://doi.org/10.1029/2011JD015901